

Article

Extrusion-Based Additive Manufacturing of the Ti6Al4V Alloy Parts

Maksim Krinitcyn ^{1,2,*} , Alexandr Pervikov ^{1,2} , Natalya Svarovskaya ^{1,2} , Alexandr Lozhkomoev ^{1,2} 
and Marat Lerner ^{1,2} 

¹ Institute of Strength Physics and Materials Science SB RAS, 634055 Tomsk, Russia

² Faculty of Physics and Engineering, Tomsk State University, 634050 Tomsk, Russia

* Correspondence: krinmax@gmail.com

Abstract: The paper shows the possibility of synthesizing microparticles coated with nanoparticles by electric explosion of a wire made of Ti-6Al-4V alloy. Particles in which the core is a microparticle and the shell of a nanoparticle can provide effective sliding of the microparticles relative to each other and are promising for obtaining flowable metal-polymer compositions filled with powder up to 70 vol.%. Such compositions are promising feedstocks for the additive molding of complex metal parts, for example, customized implants from the Ti-6Al-4V alloy, by material extrusion. The article describes the properties of feedstock based on micro- and nanoparticles of the Ti-6Al-4V alloy, the microstructure and some mechanical properties of sintered samples. The structure, bending strength and Vickers hardness of additively formed samples sintered at a temperature of 1200 °C was investigated.

Keywords: extrusion-based additive manufacturing; Ti-6Al-4V alloy; electrical explosion of wire



Citation: Krinitcyn, M.; Pervikov A.; Svarovskaya, N.; Lozhkomoev, A.; Lerner, M. Extrusion-Based Additive Manufacturing of the Ti6Al4V Alloy Parts. *Coatings* **2023**, *13*, 1067. <https://doi.org/10.3390/coatings13061067>

Academic Editor: Lyra Xing

Received: 13 April 2023

Revised: 2 June 2023

Accepted: 6 June 2023

Published: 8 June 2023



Copyright: © 2023 by the authors. Licensee MDPI, Basel, Switzerland. This article is an open access article distributed under the terms and conditions of the Creative Commons Attribution (CC BY) license (<https://creativecommons.org/licenses/by/4.0/>).

1. Introduction

Due to the complexity and high costs of manufacturing implants, it is very difficult to manufacture a customized product that takes into account the anatomical features of each patient. Additive manufacturing (AM) makes it possible to manufacture customized implants of complex shape without any additional technological operations and fixtures, using only implant CAD data and a 3D printer [1,2]. Exclusion from the process of labor-intensive and expensive technological operations allows reducing the cost of manufacturing one product and increase the production of customized implants. AM is considered as the most promising technology for the production of implantable devices customized for a specific patient [3–5].

Metallic materials with the most optimal properties for implants are titanium and alloys based on it obtained by doping a titanium matrix with elements such as Mo, Nb, Ta, Zr, Fe, V, Al, and Sn [6]. The alloy Ti-6Al-4V (abbreviated as Ti64) is most commonly used in bone replacement implants due to its high strength-to-weight ratio [7]. The alloy contains from 3.5 to 4.5 wt.% vanadium and from 5.5 to 6.75 wt.% aluminium.

Nowadays, additive manufacturing printing techniques such as selective laser melting (SLM) [8] and electron beam melting (EBM) [9] are most widely used for the manufacture of load-bearing metal implants.

SLM is a promising method for the manufacture of medical devices due to its versatility and high accuracy, as well as the good quality of the surface of implants [10–13]. EBM is another promising method for AM implants made of Ti64 [14,15]. Samples made by EBM are superior in mechanical properties compared to samples made by traditional methods [16,17].

The main disadvantages of SLM and EBM are the high price of commercial equipment, which makes it inaccessible to a large number of potential consumers. However, the advantages of AM significantly outweigh the existing disadvantages, and therefore, it seems

relevant not only to develop existing methods, but also to develop new cheaper methods for the additive production of medical parts from Ti64.

A method that may be a solution is a material extrusion-based additive manufacturing (MEAM), which is currently under active development. The method has shown high promise as an economical way to AM metal, ceramic and metal-ceramic parts [18]. In MEAM, the additive molding material is a mixture of polymer binder (usually from 40% to 60% by volume) and a fine-grained powder of the corresponding material. A mixture of polymer with powder (feedstock) can be used either in the form of granules, or in the form of a filament. The production of a metal or ceramic-metal part occurs in the same way as in PIM technology. After printing a “green” part, the polymer is removed from it by the active medium (debinding operation), and the resulting, so-called “brown” part is sintered in a high temperature vacuum furnace. The method does not impose strict requirements on the characteristics of powders and makes it possible to manufacture complex-shaped parts from various materials [19–21].

Feedstocks containing metal particles with an average size of 5 to 15 μm [22] or ceramic particles of 1 to 2 μm [23] are used in MEAM. Significant dispersion in particle sizes is an advantage of MEAM over SLM and EBM methods using powder bed technology. In SLM and EBM technologies, it is preferable to use free-flowing powders with particles of similar sizes in order to ensure reliable operation of the equipment.

The possibility of using feedstock in MEAM is determined by the viscosity of the molten material [24]. Developers tend to use readily available feedstocks for MEAM as used in PIM. At the same time, it has been shown that the viscosity of feedstocks used in PIM is very significant and, moreover, is not a constant value, but is determined by the effective shear deformations [25,26]. The high viscosity of PIM feedstocks necessitates the creation of special and expensive 3D printers, such as those made by Desktop. metal Inc. (Burlington, MA, USA) [27] and Markforged Inc. (Watertown, MA, USA) [28].

At the same time, the idea of using simple and cheap FFF printers for extrusion molding of parts continues to be relevant. However, the use of such printers requires the development of feedstocks with low viscosity and high fluidity.

The viscosity of PIM feedstock is mainly determined by the properties of the binder polymer and the ratio of binder polymer to powder. Reducing the amount of powder in the feedstock leads to a decrease in its viscosity. However, if the powder content is less than 50 vol.%, with the sinterability of the material and the density of the sintered part are significantly reduced. On the other hand, when the powder content in the feedstock is more than 65 vol.%, the viscosity of the material becomes so high that it is difficult to inject the molten feedstock into the mold [29].

Conventional FFF machines can be used when the amount of powder in the mixture compared to the polymer component is small [30]. An increase in the powder content in the feedstock, while maintaining or even reducing the viscosity of the material, is possible when using bimodal powders, which are mixtures of nano- and microparticles [31,32]. Nanoparticles located on the surface of spherical microparticles provide effective sliding of microparticles relative to each other, which makes it possible to increase feedstock fluidity at a high content of the dispersed phase. Also, mixtures of powders with different particle sizes is a promising approach to increase the density of printed and sintered parts. Interparticle voids between large particles can be filled with small particles [33]. Feedstocks based on bimodal powders of nano- and microparticles are already used in PIM and make it possible to obtain sintered parts with a relative density of at least 0.97%, and the presence of nanoparticles in the powder leads to grain refinement of the sintered material and, as a result, to an increase in its hardness [34,35]. One of the well-known methods for the synthesis of nanoparticles is electric wire explosion (EEW) [36], which also makes it possible to obtain homogeneous mixtures of nano- and microparticles [37].

In this paper, Ti64 EEW alloy powders in which nanoparticles are located on the surface of microparticles, are obtained. Development of feedstocks from synthesized powders and identification of the possibility of additive manufacturing of extrusion-based parts from

the obtained metal-polymer compositions investigated. The main purpose of this work is to obtain and investigate the Ti64 samples using bimodal nano-micro powder. These results are supposed to be used in the future to develop the technological foundations for the additive production parts using the Ti64 powder. The main novelty of this article lies in the development of a new material based on a bimodal powder for 3D printing with its full study up to the stage of forming bulk products.

2. Materials and Methods

To obtain a mixture of Ti64 nano- and microparticles, a setup described in [38] was used. The wire used in EEW had a composition of Al—5.8 wt.%, V—4.4 wt.%, the rest was Ti (the composition is specified by the manufacturer) and the following geometric parameters: diameter 0.4 mm, length 80 mm.

EEW parameters were used: the inductance of the electrical circuit $L_c \approx 0.75 \mu\text{H}$, the resistance of the electrical circuit $R_c \approx 0.08 \text{ Ohm}$, the capacitance of the capacitor bank $C \approx 2.2 \mu\text{F}$, charging voltage of the capacitor bank $U_0 = 21 \text{ kV}$. The energy inputs $E(t)$ into the wire were determined from the oscillogram of the discharge current $I(t)$ and voltage $U(t)$ by the method of replacing the integral (1) final amount.

$$E(t) = \int_0^t U(t)I(t)dt \quad (1)$$

where $U(t)$ is the time dependence of the voltage on the wire, $I(t)$ is the time dependence of the current flowing through the wire.

An electronic image of the nanoparticles was obtained using a JEM-2100 transmission electron microscope (TEM), Akishima, Tokyo, Japan. The elemental composition and distribution of elements in nanoparticles was carried out using an X-Max X-ray detector combined with a microscope. To determine the average size of nanoparticles, according to electron microscopy data, histograms of particle size distribution were built. The obtained histograms of particle size distribution were approximated by the normal-logarithmic law. To construct each histogram, the sizes of at least 3000 particles were measured. The phase composition of nanoparticles was determined using X-ray diffractometer Shimadzu XRD 6000 (Shimadzu Corporation, Tokyo, Japan) with $\text{CoK}\alpha$ radiation.

The following polymer composition was used to prepare the feedstock: EVA EA 28025 (Ethylene vinyl Acetate Copolymer) —10 wt.%, tall oil rosin —75 wt.%, dioctyl adipate —15 wt.%. The content of Ti64 powder in the polymer composition was 70 vol.%. The powder and polymers were mixed in a twin screw mixing chamber at a temperature of 150 °C. The obtained metal-polymer compositions were crushed into granules with a size of 2–4 mm. The melt flow index (MFI) of the feedstock was measured on a plastometer Zwick/Cflow at a load of 21.6 kg and a temperature of 150 °C. The study of the morphology of feedstock fractures was carried out on a scanning electron microscope (SEM) LEO EVO 50 (Carl Zeiss, Jena, Germany).

The tensile strength and elastic modulus of the filaments were determined using a DVT GP universal testing machine (Devotrans, İstanbul, Turkey). Additive manufacturing of parts was carried out on a BIZON 2 3D printer equipped with a microextruder for supplying granules and then a molten feedstock to the building zone.

Grinder ATM Saphir (QATM, Mammelzen, Germany) was used for polishing samples using 100 to 8000 grit SiC sanding paper. The structure of the samples was studied using an optical metallographic microscope Axiovert 200 MAT (Carl Zeiss, Jena, Germany) and Apreo 2 scanning electron microscope (Thermo Fisher, Waltham, MA, USA) with Energy Dispersive Spectroscopy (EDS) on built-in attachment (EDAX, Pleasanton, CA, USA). According to optical metallography, the average sizes of α -grains were measured using ImageJ software (v.1.8.0 by Wayne Rasband, NIH, Bethesda, MD, USA).

For three-point bending tests, samples with size $2 \times 2 \times 16 \text{ mm}^3$ were prepared according to ISO 7438:2020. The tests were carried out on a Gotech tensile testing machine AI-7000M (Gotech testing Machines Inc., Taichung City, Taiwan) with a loading speed of

0.5 mm/min. A series of 6 samples was tested. The fracture surfaces of the samples were examined using an Apreo 2 scanning electron microscope. The hardness of the samples was measured using a microhardness tester Duramin 500 (Struers, Copenhagen, Denmark) at 500 gf load with a 10 s dwell time.

3. Results and Discussion

3.1. Obtaining of The EEW Powders

The time dependences of $I(t)$, $U(t)$ and the energy introduced into the wire $E(t)$ are presented (Figure 1). In accordance with the classification of the time dependences of current and voltage characteristic of EEW, the explosion of the Ti64 alloy is similar to the explosion of other Group II metals with a high boiling point and high heat content at the melting temperature, for example, Fe and Ni [39]. For group II metals, the discharge current $I(t)$ reaches its maximum value by the time the conductor melts.

Titanium, as the main metal in the alloy, has the main influence on the temporal characteristics of the EEW alloy. By analogy with other Group II metals, the following characteristic times can be distinguished on the $U(t)$ and $I(t)$ curves of the Ti64 alloy. The time interval from t_0 to t_1 corresponds to the heating of the metal, then the moment of its melting t_1 . In this time interval, the current increases. The time interval from time t_1 to time t_2 corresponds to the melting of the metal. The resistance of the metal increases, limiting the current in the wire. In the time interval $t_1 - t_2$, EEW occurs, the wire is destroyed, and a dense core is formed from the explosion products, which has a foamy structure [40]. According to [36,41] during the EEW, the dispersion products (explosion products) are a mixture of liquid droplets and metallic gas.

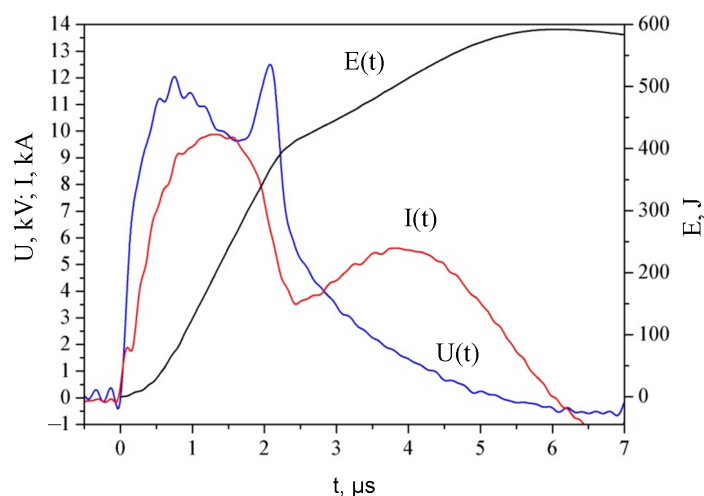


Figure 1. Time dependences of current $I(t)$, voltage $U(t)$ and energy $E(t)$ introduced into the Ti64 alloy wire.

According to [36], at $t > t_3$ an arc discharge develops in the explosion products. Thus, during the electric explosion of a wire made of Ti64 alloy with the selected parameters EEW and wire in the time interval from 0 to t_3 , the wire metal overheats to the value $E(t_3) \approx 9.0$ kJ/g, then, at $t > t_3$, an arc discharge develops and energy $E(t > t_3) \approx 4.0$ kJ/g is introduced into the wire.

The current density through the Ti64 wire reaches a value of 7.7×10^6 A/m². According to [39], explosions with a current density of 10^6 A/cm² $< j < 10^7$ A/cm² are classified as “slow” explosions. In this type of explosions, due to the heating inhomogeneity, a relatively small part of the metal evaporates before the wire breaks, and most of it is sprayed in the form of droplets, forming microparticles.

3.2. Particle Characterization

Ti64 powder obtained by EEW is represented by a homogeneous mixture of microparticles with sizes of several micrometers (Figure 2a) and nanoparticles with sizes less than 100 nm (Figure 2b). The powder also contains a certain amount of particles with sizes on the order of hundreds of nanometers (Figure 2b).

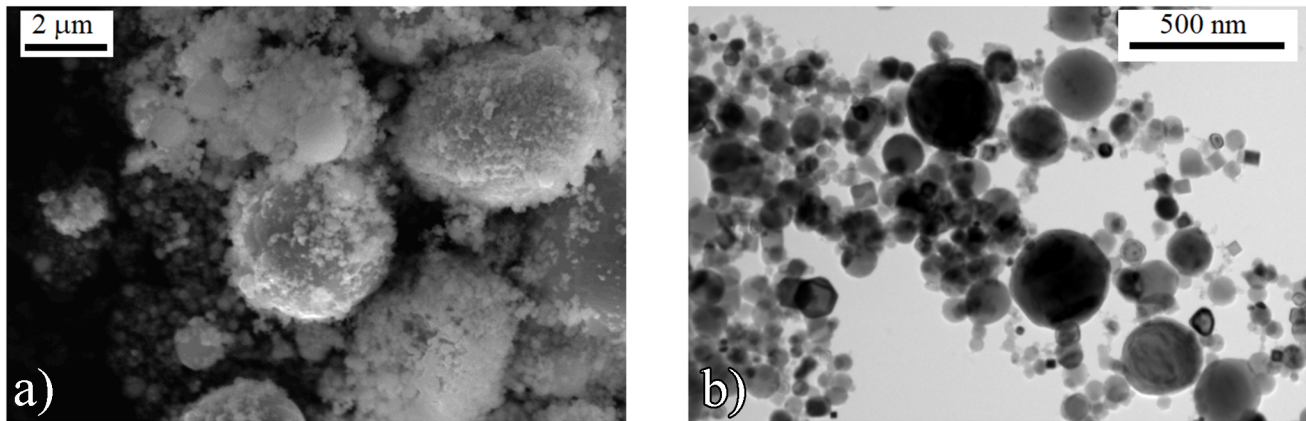


Figure 2. SEM (a) and TEM (b) images of Ti64 particles.

Nanoparticles are mainly located between microparticles, but a significant part of nanoparticles is located on the surface of microparticles, forming a shell (Figure 3).

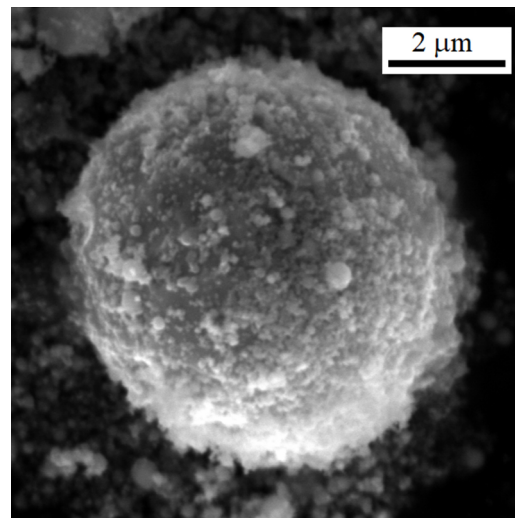


Figure 3. SEM image of a micron Ti64 particle coated with nanoparticles.

Particles with a microparticle core and nanoparticle shell (Figure 3) are important for the creation of feedstocks with high fluidity at a metal powder content of more than 60 vol.%. Nanoparticles provide interparticle sliding due to the so-called ball bearing effect [42].

The average size of nanoparticles is 75 nm (Figure 4a), the average size of microparticles is 1039 nm (Figure 4b). The distributions in Figure 4a,b shows submicron particles with sizes greater than 100 nm but less than 1 μm in addition to nanoparticles (less than 100 nm in size) and microparticles (more than 1 μm in size).

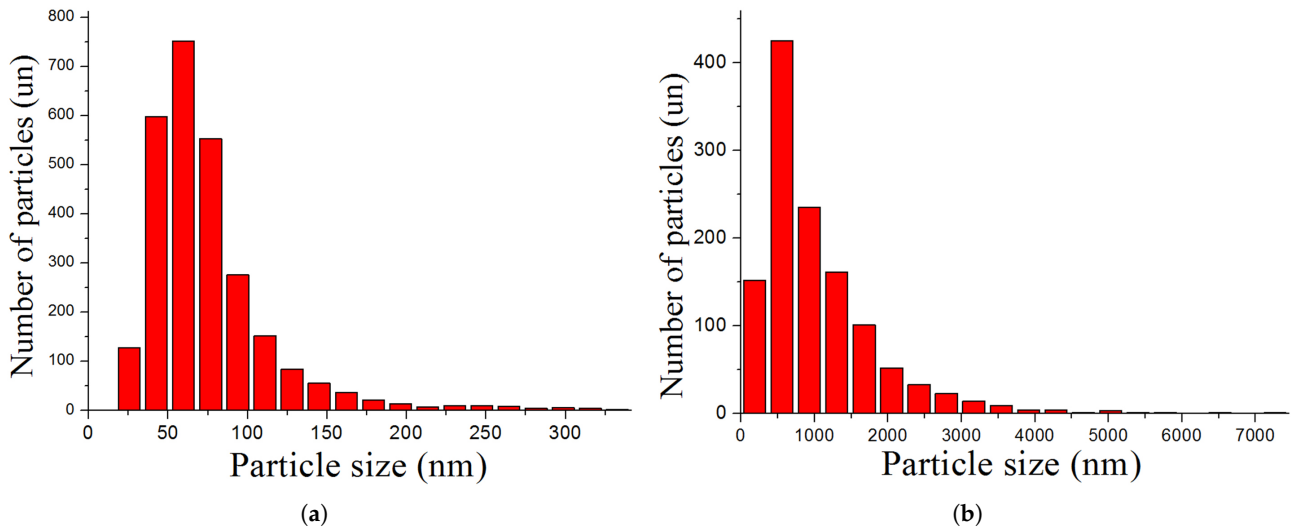


Figure 4. Distribution functions of nano- and submicron particles (a) and size distribution of microparticles (b) of Ti64.

In Figure 5 and in Table 1 the EDX elemental composition of Ti64 particles of different sizes is provided. In submicron particles larger than 100 nm (Spectrum 1, Figure 5a) and (Spectrum 1, 2, and 3, Figure 5b), there are noticeable deviations of the mass of aluminum and vanadium from the content of metals in the wire. The content of carbon and oxygen in all samples is not higher than equipment measurement error, and there are no local areas of increased concentration of these elements.

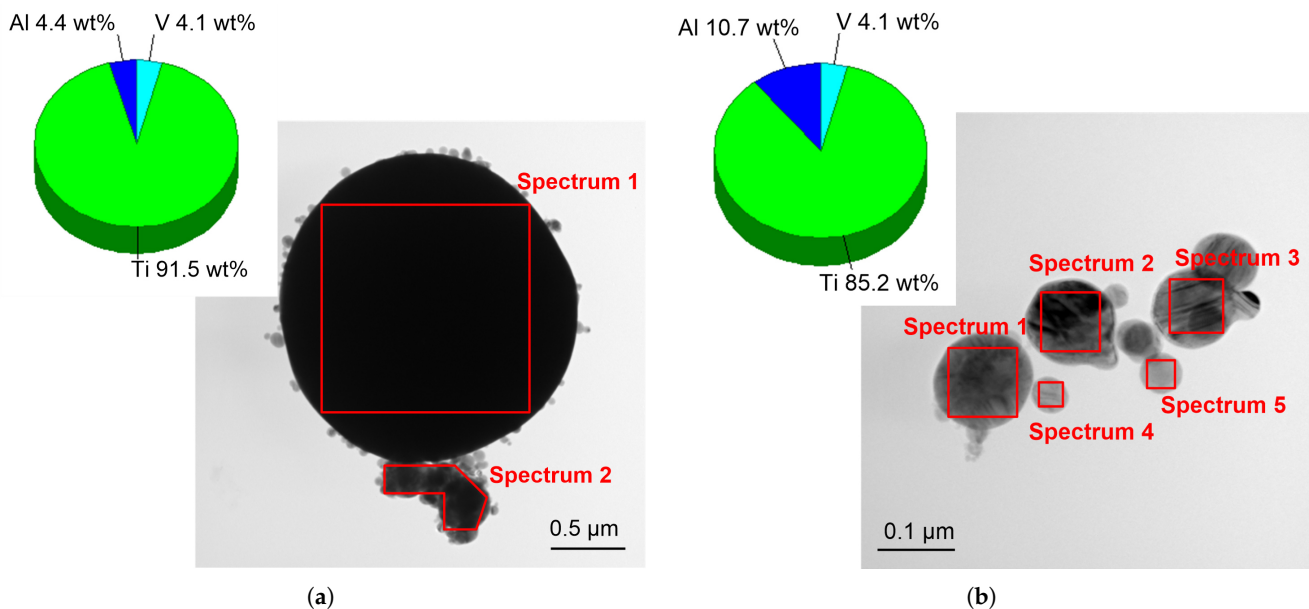


Figure 5. Elemental analysis of coarse (a) and fine (b) Ti64 particles, the pie chart shows the total content of components in the sample.

In micron-sized particles (Spectrum 1, Figure 5a), the amount of aluminum is less than its content in the wire. In most nanoparticles and submicron particles, the Al content is higher than in the wire (Spectrum 2, sample a and Spectrum 1–4, sample b, Table 1). A few nanoparticles have been found in which an excess of V has been found. Thus, when obtaining Ti64 powders by the EEW method, the initial ratio of alloy components changes in submicron particles and nanoparticles. This is due to the fact that, at the melting

temperature of Ti64, the alloy components (titanium, aluminum, and vanadium) have different vapor pressures, which can lead to the evaporation of aluminum (high vapor pressure) [43]. For example, evaporation of aluminum is observed during melting and casting of Ti64 and can lead to the production of an alloy with component ratio different from the calculated composition [44]. Due to the fact that particles of different sizes have different masses, nano- and submicron particles cooling down faster than micron-sized particles during the expansion of explosion products. Evaporation of aluminum from the surface of “hot” large particles and condensation on “cold” small particles occurs.

Table 1. Elemental composition of Ti64 particles presented in Figure 5.

Spectrum No.	Sample (a), Figure 3				Sample (b), Figure 3			
	Element, wt.%			Total, wt.%	Element, wt.%			Total, wt.%
	Ti	Al	V		Ti	Al	V	
1	90.8	4.1	4.4	100	85.2	12.9	1.9	100
2	85.9	10.6	3.5	100	85.2	9.7	5.1	100
3	—	—	—	—	88.8	8.9	2.3	100
4	—	—	—	—	83.1	14.2	2.7	100
5	—	—	—	—	82.1	6.0	11.9	100
avg.	89.0	6.3	4.7	100	84.9	10.4	4.7	100

At the same time, deviations of the aluminum content from the calculated one should be observed on a small scale (10^1 – 10^4 nm). When obtaining a bulk material, due to the volumetric diffusion of aluminum, the uniform distribution of aluminum with correct component ratios will be restored in the alloy.

3.3. Feedstock Investigation

Submicron and nanoparticles located on the surface of large particles (up to several micrometers) in feedstock Ti64 (Figure 6), as well as in powder. This structure of the feedstock ensures its high fluidity, since submicron and nanoparticles act as a solid lubricant for micron particles (ball bearing effect) [45,46]. Due to the self-lubricating effect of the powder, a higher filling of the feedstock with powder is possible. Thus, the flow rate of the feedstock melt containing 70 vol.% of Ti64 alloy powder was 57 g/10 min, which is an acceptable value for the manufacture of green parts by extrusion of the molten material.

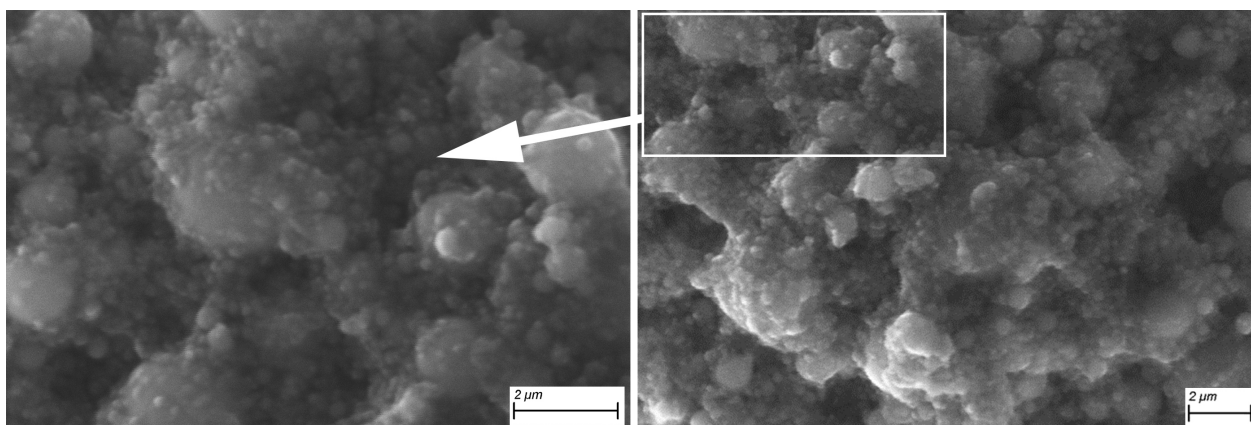


Figure 6. SEM image of the fracture surface of the Ti64 feedstock.

There are no areas of pure polymer in the feedstock—it is completely distributed over the surface of the particles. Since the feedstock contains particles in the range from nanometers to about 10^0 – 10^1 μm , the bulk density of a powder is higher than that of powders with a narrower size distribution. It is possible to reduce the size of voids that

appear in the gaps between powder particles and are a potential place for the accumulation of pure polymer.

An even distribution of the powder particles and polymer binder in the feedstock is important because it helps to minimize the segregation of components during the green part production stage and obtain isotropic shrinkage after debinding and sintering [47].

Despite the fact that granular feedstock was used to form the green part, the possibility of making filaments from the developed material was studied. The use of granular feedstocks is not always convenient, because most commercial 3D printers work with filaments. For the manufacture of filament, samples in the form of rods with a 2 mm diameter and a 50 mm length were made from a molten feedstock using a piston extruder. The tensile strength of the samples was 0.7 MPa, and the modulus of elasticity was 2.3 MPa. Obtained values of tensile strength and modulus of elasticity show the possibility of creating filaments from feedstocks with 70 vol.% powder filling, since the above properties are sufficient to ensure the process of manufacturing a filament and printing with it. The studied material was prepared in the form of a filament and successfully wound onto a spool.

Green details in the form of tablets with a 25 mm diameter and a 4.2 mm height were formed using a 3D printer with a microextruder for a granular feedstock. A nozzle with a diameter 0.6 mm was used. Debinding of green parts was carried out in acetone at 20 °C for 24 h. Weighing the tablets showed that up to 80 wt.% soluble components are dissolved.

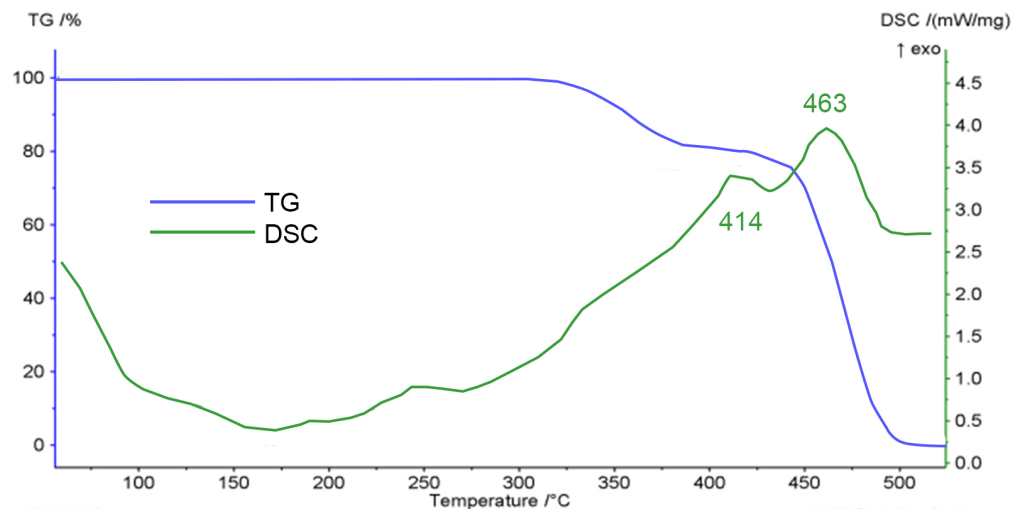
It was suggested that the rest of the polymers could be removed by sintering the samples. According to reference data, dioctyl adipate has a boiling point of 224 °C, at higher temperatures it will be completely removed. Similar data for EVA and rosin could not be found in the literature. Using differential scanning calorimetry (DSC) and thermogravimetry (TG), the decomposition temperatures of EVA and rosin were determined (Figure 7). As follows from the data (Figure 7), polymers completely decompose at temperatures above 500 °C.

3.4. Sintered Specimens Investigation

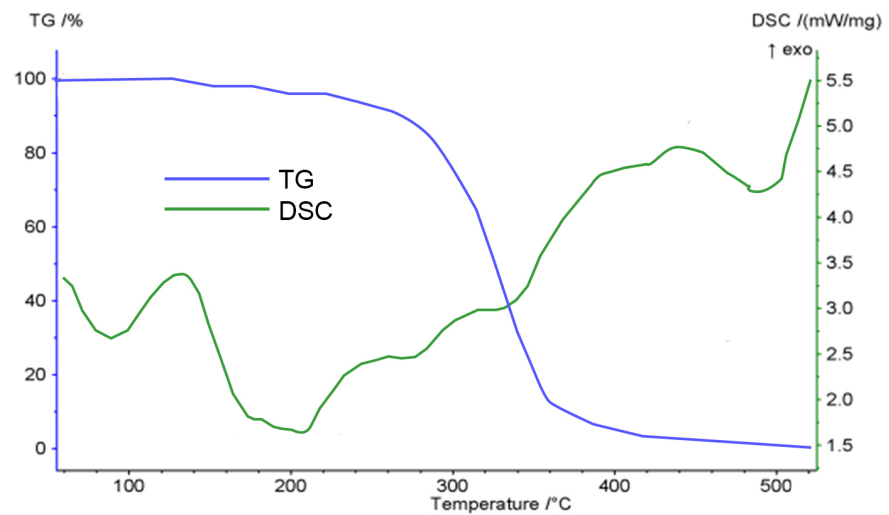
The sintering of the tablets was carried out in a vacuum furnace (10^{-6} Pa) at a temperature of 1200 °C for 24 h. In sintered samples, a globular structure of α -grains surrounded by veinlets of the β -phase is observed (Figure 8). The average size of α -grains is 12.5 ± 0.5 μm . This structure is typical for titanium α - β alloys sintered at temperatures below the β transition temperature (about 900 °C) [48]. However, in the studied samples, globular structure is retained after sintering at 1200 °C.

During sintering, a lamellar structure is formed in the samples; the globular structure can remain locally. It is also possible to form a duplex structure [49,50], where the α -phase is equally present both in the form of rounded grains and in lamellar form. The formation of a duplex structure also occurs at temperatures below the β -transition.

In accordance with [48], lamellar colonies of α -particles are just beginning to form in samples (Figure 9a,b)—along the boundaries of α -grains towards the β -phase, individual needle-like lamellae no longer than 2 μm begin to grow. There are dark marks in the figure, which are the results of mechanical processing of the samples. The porosity of the samples, measured by hydrostatic weighing, is 98% of the theoretical one. Porosity is mainly formed due to single production defects and can be reduced.



(a)



(b)

Figure 7. Thermal properties of polymers: (a) TG/DSC EVA, (b) TG/DSC rosin.

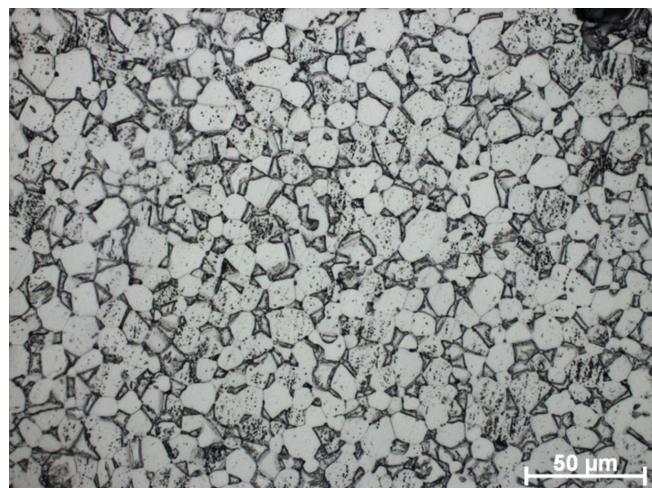


Figure 8. Cross-sectional optical microscopy of the sintered Ti64 sample.

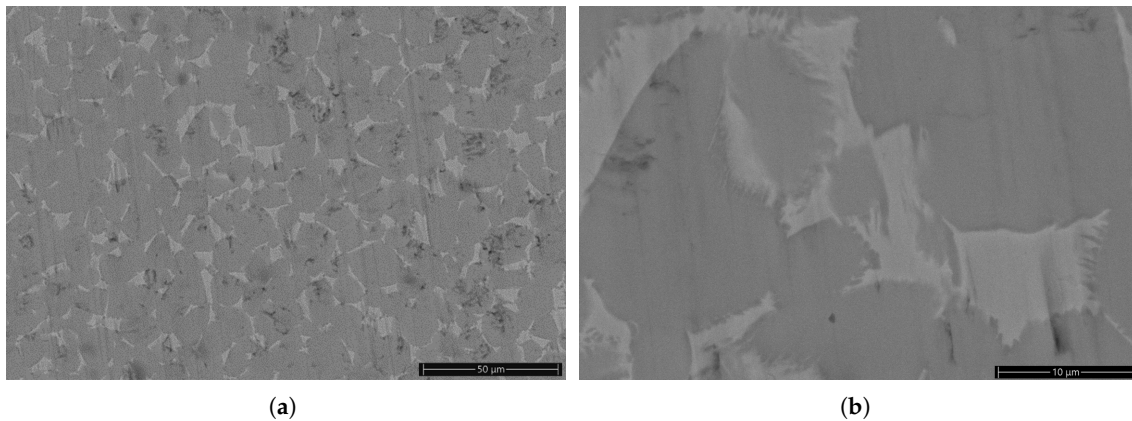


Figure 9. Cross-sectional SEM pictures of the sintered Ti64 samples at low (a) and high (b) magnification.

It follows from elemental analysis that the metal phases are evenly distributed in the sintered part (Figure 10). In this case, the regions of the α -phase mainly consist of titanium, while Al and V are concentrated in the region of the β -phase. The elemental analysis from the area shows that the content of components in the Ti64 sample after sintering nearly corresponds to their content in the wire Al = $5.7 \pm 0.5\%$, V = $4.2 \pm 0.5\%$. The distribution of the alloy components in the particles obtained in the EEW are differing from the specified one, but it does not affect the distribution of the components in the sintered bulk alloy.

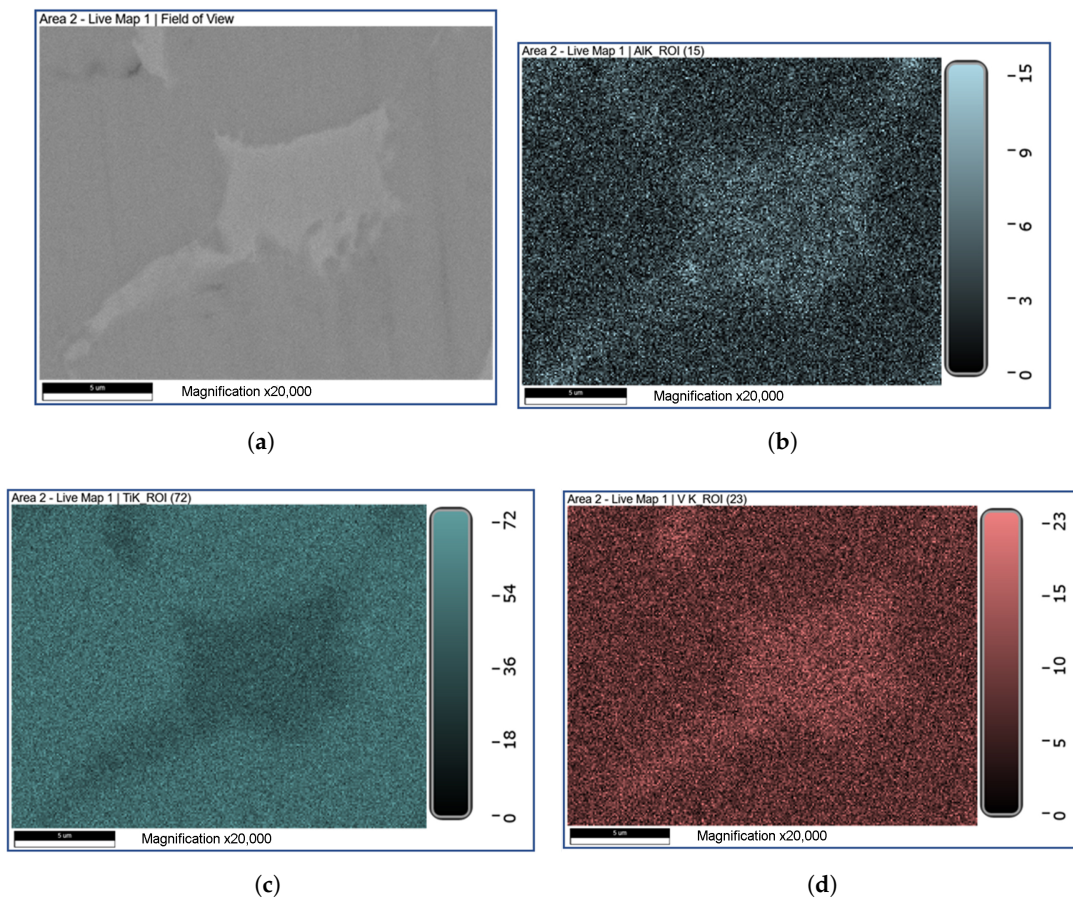


Figure 10. Elemental analysis of the sintered Ti64 sample: (a) image section, (b) aluminum, (c) titanium, (d) vanadium.

3.5. Mechanical Properties

Vickers hardness for the samples is 806 ± 23 HV, which is higher than the values for the pure alloy [51–53] and corresponds to the dispersion-hardened Ti64 alloy [54].

The average bending strength of the samples is 182 ± 16 MPa, which is clearly insufficient for the manufacture of implantable devices. Brittle fracture of the specimens occurs (Figure 11)—the deformation takes place in the elastic region, the loading curve is almost linear, then there is a destruction of the specimen.

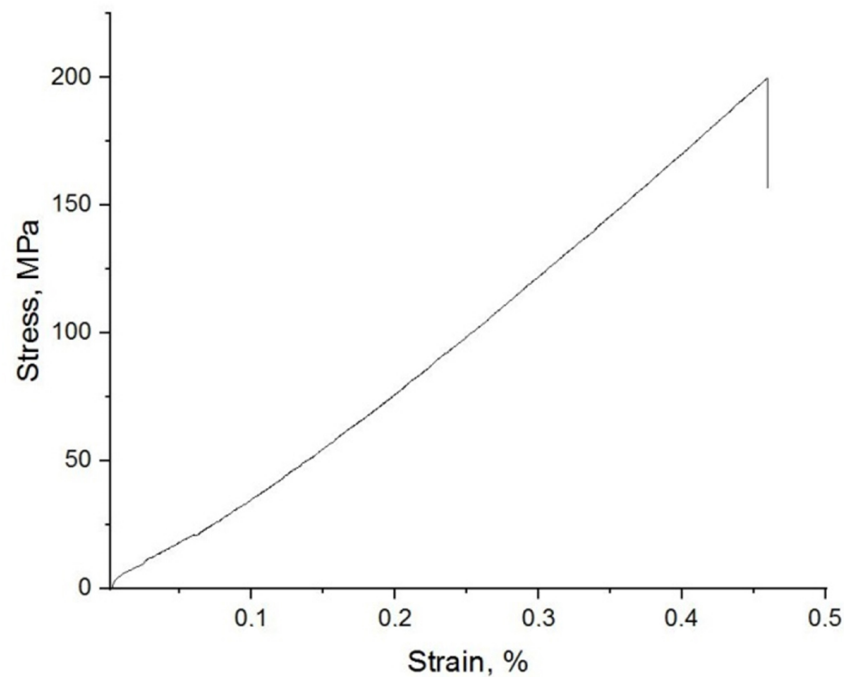


Figure 11. Stress-strain curve of the sintered Ti64 sample.

The brittle nature of the fracture is confirmed by the study of fractograms (Figure 12)—no areas of ductile fracture are observed. Fracture proceeds along the grain boundaries of the β -phase, as evidenced by the relief areas on the fracture surface. The grains of the α -phase are destroyed along the boundaries, but intragranular cleavage is observed, as can be seen from the lamellar structures.

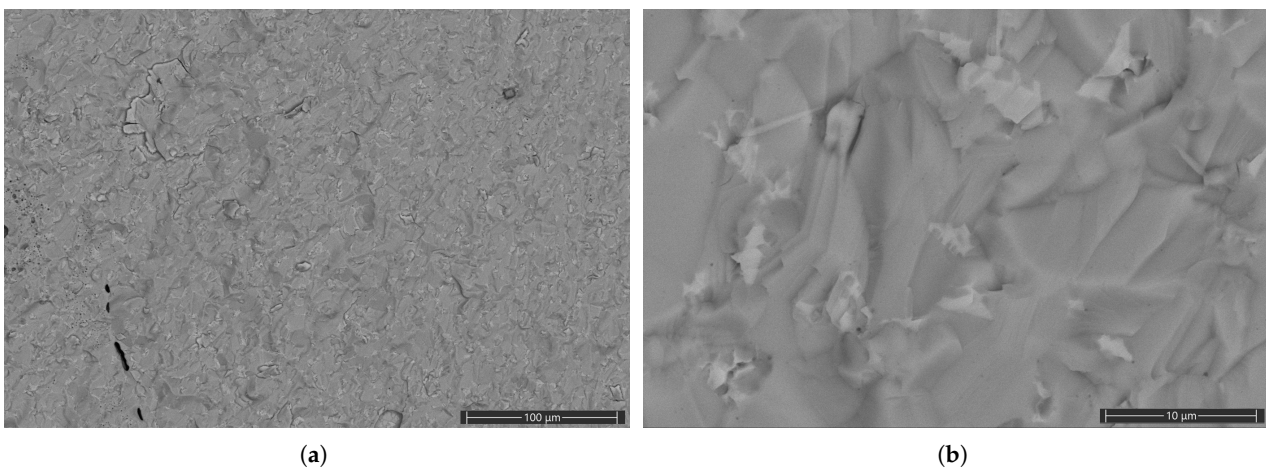


Figure 12. Fracture surfaces of the sintered and bent Ti64 sample at low (a) and high (b) magnification.

Ti64 alloy with a globular structure is characterized by a higher strength compared to a lamellar structure, including in cyclic fatigue testing. Also, the globular structure is characterized by low fracture toughness, which is observed in this case.

Preservation of the globular structure despite the high (1200 °C) sintering temperature is possible as a result of two main factors. The first factor is the small size of the initial powders. During the sintering of fine powders, α -grain growth initially occurs, which shifts the growth of α -lamellae colonies to a higher temperature region.

The second and more significant factor is the presence of dissolved impurities in the alloy. Since the material was formed from a metal-polymer composition, impurities containing carbon may remain on the surface of the powder particles after debinding. The thermal removal of the polymer binder occurs at temperatures above 500 °C, which is sufficient to start the dissolution of carbon in titanium [55]. Elements such as carbon, nitrogen and oxygen interact with titanium actively and can dissolve in it, including without the formation of crystalline phases and be in interstices (dissolution according to the interstitial principle) [56–59]. The presence of carbon in titanium in an amount of 0.1% or more leads to its embrittlement [60].

Thus, during the formation of a feedstock, a polymer layer is formed on the surface of nanosized and submicron Ti64 alloy particles, which is not completely removed after debinding. An obligatory component of the feedstock is a backbone polymer, which is removed only at high temperatures (about 500 °C), which are already sufficient to start the dissolution of carbon in titanium. With a further increase in temperature, the sintering process is activated and grain growth begins. In this case, the powder particles are combined due to sintering and form grains of a larger size.

Dissolved carbon prevents the growth of α -grain colonies and the rearrangement of the structure into a lamellar structure during the β -transition. Researchers achieved a similar effect when introducing nanosized TiN additives into the Ti64 alloy—after sintering at a temperature of 1100 °C, the globular structure was retained, or a duplex structure began to form [61].

Carbon, initially dissolved on the surface of nano- and submicron particles, is found deep inside the formed grains, forming clusters of crystalline defects. Since acicular structures begin to form in some places of the α - β boundaries (Figure 9), the strength of the interfacial connection is higher than the intragranular strength, reduced due to the introduced carbon. In such areas, the destruction occurs inside the grains (Figure 12).

EVA is probably responsible for the carbonization of the alloy, which, unlike rosin and dioctyl adipate, can form soot during sintering, due to incomplete destruction.

4. Conclusions

Electric explosion of a Ti64 wire belongs to the II group according to the accepted classification. In this type of explosions, due to the inhomogeneity of heating, a relatively small part of the metal evaporates before the wire explodes, and most of it is sprayed in the form of droplets, which makes it possible to obtain homogeneous mixtures of nano- and microparticles. The resulting powder consists of microparticles, mainly coated with nanoparticles and submicron particles.

During EEW a redistribution of aluminum between large and small particles occurs, as a result of which fine particles contain an excess of metal. However, during sintering of the samples, no violation of the homogeneity of the material composition is observed. Probably, diffusion occurs as a result of prolonged heating of the samples in a vacuum. Alignment of the concentrations of the components takes place throughout the volume of the sintered material.

The possibility of creating feedstocks highly filled with powder (70 vol.%) based on microparticles coated with nanoparticles for additive molding of parts using the extrusion-based method is shown. Feedstock developed on the basis of Ti-6Al-4V powders have fluidity sufficient for extrusion of molten material and mechanical properties that allow creating filaments based on it.

In samples sintered at a temperature of 1200 °C, a globular structure of α -grains with an average size of $12.5 \pm 0.5 \mu\text{m}$ is formed. Such a structure is characteristic of specimens sintered at temperatures below the β -transition temperature. The fracture of the samples is completely brittle, the bending strength of the samples is $182 \pm 16 \text{ MPa}$, and the Vickers hardness is $806 \pm 23 \text{ HV}$. This complex of structural and mechanical characteristics of the alloy is formed due to the dissolution of carbon in it from the residual polymer, which leads to dispersion strengthening and embrittlement of the material.

For further development of additive molding of parts of complex shape from Ti-6Al-4V extrusion-based additive manufacturing are required to improve the mechanical characteristics of sintered parts. To do this, it is necessary to prevent the carburization of the alloy during its sintering, which requires the replacement of EVA with a polymer that does not give residual carbon when heated (for example, linear polyethylene, etc.).

Author Contributions: Conceptualization and experimental design, M.K., A.P., N.S., A.L. and M.L.; methodology, analysis, and discussion of the results, A.P., N.S. and A.L.; manuscript writing, M.K. and M.L. All authors have read and agreed to the published version of the manuscript.

Funding: The research was performed at the financial support of grant of Russian Science Foundation (project No. 21-79-30006), <https://rscf.ru/en/project/21-79-30006/>.

Data Availability Statement: The data presented in this study are available on request from the corresponding author.

Conflicts of Interest: The authors declare no conflict of interest.

References

1. Bandyopadhyay, A.; Bose, S.; Das, S. 3D printing of biomaterials. *MRS Bull.* **2015**, *40*, 108–115. [[CrossRef](#)]
2. Tetsworth, K.; Block, S.; Glatt, V. Putting 3D modelling and 3D printing into practice: Virtual surgery and preoperative planning to reconstruct complex post-traumatic skeletal deformities and defects. *SICOT-J* **2017**, *3*, 16. [[CrossRef](#)] [[PubMed](#)]
3. Van der Stok, J.; Van der Jagt, O.P.; Amin Yavari, S.; De Haas, M.F.; Waarsing, J.H.; Jahr, H.; Van Lieshout, E.M.; Patka, P.; Verhaar, J.A.; Zadpoor, A.A.; et al. Selective laser melting-produced porous titanium scaffolds regenerate bone in critical size cortical bone defects. *J. Orthop. Res.* **2013**, *31*, 792–799. [[CrossRef](#)] [[PubMed](#)]
4. Li, C.; Pisignano, D.; Zhao, Y.; Xue, J. Advances in medical applications of additive manufacturing. *Engineering* **2020**, *6*, 1222–1231. [[CrossRef](#)]
5. Novakov, T.; Jackson, M.; Robinson, G.; Ahmed, W.; Phoenix, D. Laser sintering of metallic medical materials—A review. *Int. J. Adv. Manuf. Technol.* **2017**, *93*, 2723–2752. [[CrossRef](#)]
6. Zhecheva, A.; Sha, W.; Malinov, S.; Long, A. Enhancing the microstructure and properties of titanium alloys through nitriding and other surface engineering methods. *Surf. Coatings Technol.* **2005**, *200*, 2192–2207. [[CrossRef](#)]
7. Gupta, J.; Ghosh, S.; Aravindan, S. Effect of Mo and space holder content on microstructure, mechanical and corrosion properties in Ti6AlxMo based alloy for bone implant. *Mater. Sci. Eng. C* **2021**, *123*, 111962. [[CrossRef](#)]
8. Yan, C.; Hao, L.; Hussein, A.; Young, P. Ti-6Al-4V triply periodic minimal surface structures for bone implants fabricated via selective laser melting. *J. Mech. Behav. Biomed. Mater.* **2015**, *51*, 61–73. [[CrossRef](#)]
9. Zadpoor, A.A.; Malda, J. Additive manufacturing of biomaterials, tissues, and organs. *Ann. Biomed. Eng.* **2017**, *45*, 1–11. [[CrossRef](#)]
10. Pattanayak, D.K.; Fukuda, A.; Matsushita, T.; Takemoto, M.; Fujibayashi, S.; Sasaki, K.; Nishida, N.; Nakamura, T.; Kokubo, T. Bioactive Ti metal analogous to human cancellous bone: Fabrication by selective laser melting and chemical treatments. *Acta Biomater.* **2011**, *7*, 1398–1406. [[CrossRef](#)]
11. Wu, S.H.; Li, Y.; Zhang, Y.Q.; Li, X.K.; Yuan, C.F.; Hao, Y.L.; Zhang, Z.Y.; Guo, Z. Porous titanium-6 aluminum-4 vanadium cage has better osseointegration and less micromotion than a poly-ether-ether-ketone cage in sheep vertebral fusion. *Artif. Organs* **2013**, *37*, E191–E201. [[CrossRef](#)] [[PubMed](#)]
12. Tunchel, S.; Blay, A.; Kolerman, R.; Mijiritsky, E.; Shibli, J.A. 3D printing/additive manufacturing single titanium dental implants: A prospective multicenter study with 3 years of follow-up. *Int. J. Dent.* **2016**, *2016*, 8590971. [[CrossRef](#)] [[PubMed](#)]
13. Muthuramalingam, T.; Moiduddin, K.; Akash, R.; Krishnan, S.; Mian, S.H.; Ameen, W.; Alkhalefah, H. Influence of process parameters on dimensional accuracy of machined Titanium (Ti-6Al-4V) alloy in Laser Beam Machining Process. *Opt. Laser Technol.* **2020**, *132*, 106494. [[CrossRef](#)]
14. Liu, P.C.; Yang, Y.J.; Liu, R.; Shu, H.X.; Gong, J.P.; Yang, Y.; Sun, Q.; Wu, X.; Cai, M. A study on the mechanical characteristics of the EBM-printed Ti-6Al-4V LCP plates in vitro. *J. Orthop. Surg. Res.* **2014**, *9*, 106. [[CrossRef](#)] [[PubMed](#)]
15. Petrovic, V.; Haro, J.V.; Blasco, J.R.; Portolés, L. Additive manufacturing solutions for improved medical implants. *Biomedicine* **2012**, *2012*, 147–180.

16. Murr, L.E.; Gaytan, S.M.; Martinez, E.; Medina, F.; Wicker, R.B. Next generation orthopaedic implants by additive manufacturing using electron beam melting. *Int. J. Biomater.* **2012**, *2012*, 245727. [[CrossRef](#)]
17. Seifi, M.; Dahar, M.; Aman, R.; Harrysson, O.; Beuth, J.; Lewandowski, J.J. Evaluation of orientation dependence of fracture toughness and fatigue crack propagation behavior of as-deposited ARCAM EBM Ti-6Al-4V. *Jom* **2015**, *67*, 597–607. [[CrossRef](#)]
18. Gonzalez-Gutierrez, J.; Cano, S.; Schuschnigg, S.; Kukla, C.; Sapkota, J.; Holzer, C. Additive manufacturing of metallic and ceramic components by the material extrusion of highly-filled polymers: A review and future perspectives. *Materials* **2018**, *11*, 840. [[CrossRef](#)]
19. Kukla, C.; Gonzalez-Gutierrez, J.; Cano, S.C.; Hampel, S.; Burkhardt, C.; Moritz, T.; Holzer, C. Fused filament fabrication (FFF) of PIM feedstocks. In *Iberoamericano de Pulvimetalurgia; Comité Español de Pulvimetalurgia: Ciudad Real, Spain, 2017*; pp. 1–6.
20. Lengauer, W.; Duretek, I.; Fürst, M.; Schwarz, V.; Gonzalez-Gutierrez, J.; Schuschnigg, S.; Kukla, C.; Kitzmantel, M.; Neubauer, E.; Lieberwirth, C.; et al. Fabrication and properties of extrusion-based 3D-printed hardmetal and cermet components. *Int. J. Refract. Met. Hard Mater.* **2019**, *82*, 141–149. [[CrossRef](#)]
21. Cruz, N.; Santos, L.; Vasco, J.; Barreiros, F. Binder system for fused deposition of metals. In Proceedings of the Euro PM2013, Congress & Exhibition, Gothenburg, Sweden, 15–18 September 2013; pp. 79–84.
22. González-Gutiérrez, J.; Stringari, G.B.; Emri, I. Powder injection molding of metal and ceramic parts. In *Some Critical Issues for Injection Molding; Books on Demand: Norderstedt, Germany, 2012*; pp. 65–88.
23. Stanimirović, Z.; Stanimirović, I. Ceramic injection molding. In *Some Critical Issues for Injection Molding; Books on Demand: Norderstedt, Germany, 2012*; pp. 131–148.
24. Venkataraman, N.; Rangarajan, S.; Matthewson, M.; Harper, B.; Safari, A.; Danforth, S.; Wu, G.; Langrana, N.; Guceri, S.; Yardimci, A. Feedstock material property–process relationships in fused deposition of ceramics (FDC). *Rapid Prototyp. J.* **2000**, *6*, 244–253. [[CrossRef](#)]
25. Park, S.J.; Kim, D.; Lin, D.; Park, S.J.; Ahn, S. Rheological characterization of powder mixture including a space holder and its application to metal injection molding. *Metals* **2017**, *7*, 120. [[CrossRef](#)]
26. Korotchenko, A.Y.; Khilkov, D.; Tverskoy, M. The development of new materials and modes of casting metal powder mixtures (MIM technology). In *Materials Science Forum; Trans Tech Publications Ltd.: Stafa-Zurich, Switzerland, 2019; Volume 945*, pp. 538–542.
27. Wohlers, T. Desktop metal: A rising star of metal AM targets speed, cost and high-volume production. *Met. AM* **2017**, *3*, 89–94.
28. Campbell, I.; Wohlers, T. Markforged: Taking a different approach to metal Additive Manufacturing. *Met. AM* **2017**.
29. Merz, L.; Rath, S.; Piottter, V.; Ruprecht, R.; Ritzhaupt-Kleissl, J.; Hausselt, J. Feedstock development for micro powder injection molding. *Microsyst. Technol.* **2002**, *8*, 129–132. [[CrossRef](#)]
30. Kalita, S.J.; Bose, S.; Hosick, H.L.; Bandyopadhyay, A. Development of controlled porosity polymer-ceramic composite scaffolds via fused deposition modeling. *Mater. Sci. Eng. C* **2003**, *23*, 611–620. [[CrossRef](#)]
31. Onbattuvelli, V.P.; Enneti, R.K.; Park, S.J.; Atre, S.V. The effects of nanoparticle addition on SiC and AlN powder–polymer mixtures: Packing and flow behavior. *Int. J. Refract. Met. Hard Mater.* **2013**, *36*, 183–190. [[CrossRef](#)]
32. Müller, M.; Bauer, W.; Kleissl, H. Low-pressure injection molding of ceramic micro devices using sub-micron and nano scaled powders. *Multi-Mater. Micro Manuf.* **2005**, 1–4.
33. Du, W.; Singh, M.; Singh, D. Binder jetting additive manufacturing of silicon carbide ceramics: Development of bimodal powder feedstocks by modeling and experimental methods. *Ceram. Int.* **2020**, *46*, 19701–19707. [[CrossRef](#)]
34. Oh, J.W.; Bollina, R.; Lee, W.S.; Park, S.J. Effect of nanopowder ratio in bimodal powder mixture on powder injection molding. *Powder Technol.* **2016**, *302*, 168–176. [[CrossRef](#)]
35. Pervikov, A.; Rodkevich, N.; Glazkova, E.; Lerner, M. Bimodal metal micro-nanopowders for powder injection molding. In *AIP Conference Proceedings; AIP Publishing LLC: Melville, NY, USA, 2017; Volume 1915*, p. 040045.
36. Kotov, Y.A. Electric explosion of wires as a method for preparation of nanopowders. *J. Nanoparticle Res.* **2003**, *5*, 539–550. [[CrossRef](#)]
37. Pervikov, A.; Toropkov, N.; Kazantsev, S.; Bakina, O.V.; Glazkova, E.; Lerner, M. Preparation of nano/micro bimodal aluminum powder by electrical explosion of wires. *Materials* **2021**, *14*, 6602. [[CrossRef](#)] [[PubMed](#)]
38. Lozhkomoiev, A.; Pervikov, A.; Kazantsev, S.; Sharipova, A.; Rodkevich, N.; Toropkov, N.; Suliz, K.; Svarovskaya, N.; Kondranova, A.; Lerner, M. Synthesis of Fe/Fe₃O₄ core-shell nanoparticles by electrical explosion of the iron wire in an oxygen-containing atmosphere. *J. Nanoparticle Res.* **2021**, *23*, 73. [[CrossRef](#)]
39. Chace, W.G.; Moore, H.K. *Exploding Wires: Volume 4*; Springer: Berlin/Heidelberg, Germany, 2014; Volume 4.
40. Baksht, R.; Tkachenko, S.; Romanova, V.; Mingaleev, A.; Oreshkin, V.; Ter-Oganes'yan, A.; Khattatov, T.; Shelkovenko, T.; Pikuz, S. Stratification dynamics and the development of electrothermal instability at the wire explosion. *Tech. Phys.* **2013**, *58*, 1129–1137. [[CrossRef](#)]
41. Sindhu, T.; Sarathi, R.; Chakravarthy, S.R. Understanding nanoparticle formation by a wire explosion process through experimental and modelling studies. *Nanotechnology* **2007**, *19*, 025703. [[CrossRef](#)] [[PubMed](#)]
42. Choi, J.P.; Lyu, H.G.; Lee, W.S.; Lee, J.S. Investigation of the rheological behavior of 316L stainless steel micro-nano powder feedstock for micro powder injection molding. *Powder Technol.* **2014**, *261*, 201–209. [[CrossRef](#)]
43. Smalcerz, A.; Blacha, L.; Łabaj, J. Aluminium loss during Ti-Al-X alloy smelting using the VIM technology. *Arch. Foundry Eng.* **2021**, *21*, 11–17.

44. Siwiec, G. The kinetics of aluminium evaporation from the Ti-6Al-4V alloy. *Arch. Metall. Mater.* **2013**, *58*, 1155–1160. [[CrossRef](#)]
45. Choi, J.P.; Park, J.S.; Hong, E.J.; Lee, W.S.; Lee, J.S. Analysis of the rheological behavior of Fe trimodal micro-nano powder feedstock in micro powder injection molding. *Powder Technol.* **2017**, *319*, 253–260. [[CrossRef](#)]
46. You, W.K.; Choi, J.P.; Yoon, S.M.; Lee, J.S. Low temperature powder injection molding of iron micro-nano powder mixture. *Powder Technol.* **2012**, *228*, 199–205. [[CrossRef](#)]
47. Quinard, C.; Barriere, T.; Gelin, J. Development and property identification of 316L stainless steel feedstock for PIM and μ PIM. *Powder Technol.* **2009**, *190*, 123–128. [[CrossRef](#)]
48. Wang, Y.Z.; Ma, N.; Chen, Q.; Zhang, F.; Chen, S.; Chang, Y. Predicting phase equilibrium, phase transformation, and microstructure evolution in titanium alloys. *Jom* **2005**, *57*, 32–39. [[CrossRef](#)]
49. Meyer, L.W.; Kruger, L.; Sommer, K.; Halle, T.; Hockauf, M. Dynamic strength and failure behavior of titanium alloy Ti-6Al-4V for a variation of heat treatments. *Mech. Time-Depend. Mater.* **2008**, *12*, 237–247. [[CrossRef](#)]
50. Heckel, T.K.; Christ, H.J. Isothermal and thermomechanical fatigue of titanium alloys. *Procedia Eng.* **2010**, *2*, 845–854. [[CrossRef](#)]
51. Wu, S.; Lu, Y.; Gan, Y.; Huang, T.; Zhao, C.; Lin, J.; Guo, S.; Lin, J. Microstructural evolution and microhardness of a selective-laser-melted Ti-6Al-4V alloy after post heat treatments. *J. Alloys Compd.* **2016**, *672*, 643–652. [[CrossRef](#)]
52. Zhang, L.C.; Attar, H. Selective laser melting of titanium alloys and titanium matrix composites for biomedical applications: A review. *Adv. Eng. Mater.* **2016**, *18*, 463–475. [[CrossRef](#)]
53. Lekoadi, P.; Tlotleng, M.; Annan, K.; Maledi, N.; Masina, B. Evaluation of heat treatment parameters on microstructure and hardness properties of high-speed selective laser melted Ti6Al4V. *Metals* **2021**, *11*, 255. [[CrossRef](#)]
54. Carquigny, S.; Takadoun, J.; Ivanescu, S. Comparative study of nitrogen implantation effect on mechanical and tribological properties of Ti-6Al-4V and Ti-10Zr-10Nb-5Ta alloys. *Eur. Phys. J. Appl. Phys.* **2019**, *85*, 21301. [[CrossRef](#)]
55. Van Loo, F.; Bastin, G. On the diffusion of carbon in titanium carbide. *Metall. Trans. A* **1989**, *20*, 403–411. [[CrossRef](#)]
56. Nakamichi, S.; Tsurekawa, S.; Morizono, Y.; Watanabe, T.; Nishida, M.; Chiba, A. Diffusion of carbon and titanium in γ -iron in a magnetic field and a magnetic field gradient. *J. Mater. Sci.* **2005**, *40*, 3191–3198. [[CrossRef](#)]
57. Rosa, C.J. Oxygen diffusion in alpha and beta titanium in the temperature range of 932 to 1142 °C. *Metall. Trans.* **1970**, *1*, 2517–2522. [[CrossRef](#)]
58. Lengauer, W. Properties of bulk δ -TiN_{1-x} prepared by nitrogen diffusion into titanium metal. *J. Alloys Compd.* **1992**, *186*, 293–307. [[CrossRef](#)]
59. Casadebaigt, A.; Hugues, J.; Monceau, D. High temperature oxidation and embrittlement at 500–600 °C of Ti-6Al-4V alloy fabricated by Laser and Electron Beam Melting. *Corros. Sci.* **2020**, *175*, 108875. [[CrossRef](#)]
60. Solonina, O.; Ulyakova, N. Effect of carbon on the mechanical properties and structure of titanium alloys. *Met. Sci. Heat Treat.* **1974**, *16*, 310–312. [[CrossRef](#)]
61. Falodun, O.; Obadele, B.; Oke, S.; Maja, M.; Olubambi, P. Synthesis of Ti-6Al-4V alloy with nano-TiN microstructure via spark plasma sintering technique. In *IOP Conference Series: Materials Science and Engineering*; IOP Publishing: Bristol, UK, 2017; Volume 272, p. 012029.

Disclaimer/Publisher’s Note: The statements, opinions and data contained in all publications are solely those of the individual author(s) and contributor(s) and not of MDPI and/or the editor(s). MDPI and/or the editor(s) disclaim responsibility for any injury to people or property resulting from any ideas, methods, instructions or products referred to in the content.